

Stress Isotropization in Weakly Jammed Granular Packings

Félix Benoist,^{1,2,*} Mehdi Bouzid,³ and Martin Lenz^{1,4,†}

¹Université Paris-Saclay, CNRS, LPTMS, 91400, Orsay, France

²Instituto Gulbenkian de Ciência, Oeiras, Portugal

³Université Grenoble Alpes, CNRS, Grenoble INP, 3SR, 38000 Grenoble, France

⁴PMMH, CNRS, ESPCI Paris, PSL University,

Sorbonne Université, Université de Paris, F-75005, Paris, France

When sheared, granular media experience localized plastic events known as shear transformations which generate anisotropic internal stresses. Under strong confining pressure, the response of granular media to local force multipoles is essentially linear, resulting in quadrupolar propagated stresses. This can lead to additional plastic events along the direction of relative stress increase. Closer to the unjamming transition however, as the confining pressure and the shear modulus vanish, nonlinearities become relevant. Yet, the consequences of these nonlinearities on the stress response to plastic events remains poorly understood. We show with granular dynamics simulations that this brings about an isotropization of the propagated stresses, in agreement with a previously developed continuum elastic model. This could significantly modify the yielding transition of weakly-jammed amorphous media, which has been conceptualized as an avalanche of such plastic events.

Introduction. When subjected to large enough macroscopic shear stress, amorphous solids such as granular packings, foams, metallic glasses or toothpaste start to flow [1, 2]. This yielding transition originates in microscopic events where the material locally undergoes a plastic deformation [3]. Each of these so-called shear transformations induces new microscopic stresses in its surroundings, which can then trigger further shear transformations. Above a critical macroscopic stress, the catastrophic accumulation of such events causes the whole material to yield and transition from a solid-like to a fluid-like behavior.

This yielding transition has been extensively studied through mesoscopic elasto-plastic models [1, 4–9]. The universality class of this yielding transition is predicated on the propagator which dictates the distribution of additional stresses induced by a new shear transformation. Linearly elastic solids display a so-called Eshelby propagator, whose quadrupolar symmetry ensures that a shear transformation induces equal amounts of positive and negative stresses in its surroundings [10, 11]. This symmetry, associated with the dipolar deformation field illustrated in Fig. 1(a,b), dictates the critical exponents at the yielding transition. Among them, the Herschel-Bulkley exponent describes how abruptly the material starts to flow once the macroscopic stress exceeds its critical value [6, 12]. Additional features such as the formation of shear bands and ageing have also been proposed to directly result from the form of the Eshelby propagator [13–15].

While the validity of the Eshelby propagator is well established in dense amorphous solids [18], looser packings may display more complex responses. Experiments on weakly-jammed emulsions [19, 20] thus indicate a non-Eshelby propagator, whereby the change in local stress surrounding a shear transformation has the same sign in all directions [17]. Similarly, an isotropic core is observed in the displacement response from force dipoles of simu-

lated harmonic sphere packings near unjamming [21]. In this article, we propose that such deviations from the Eshelby propagator are generically expected for amorphous

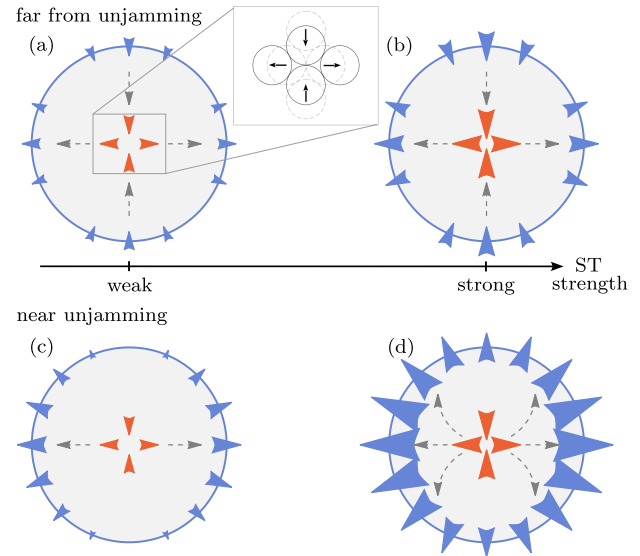


FIG. 1. The far-field stresses induced by a shear transformation (ST) become more isotropic near unjamming. (a) In an amorphous medium, a shear transformation, *e.g.*, a local change of neighbors between grains (inset) [16, 17], applies a local force dipole (orange arrowheads) on the surrounding medium (grey arrows), resulting in stresses at the medium's boundary (blue arrowheads). (b) Far from unjamming, the medium propagates stresses according to linear elasticity. The symmetry of these boundary stresses thus does not depend on the magnitude of the local forces. (c) Close to unjamming, the medium may not support the propagation of tensile stresses, resulting in a preponderance of dilational boundary stresses. (d) For large local forces, stress redistribution within the medium results in an increasingly isotropic dilation.

solids close to unjamming.

Our approach is based on the observation that as an isotropic material approaches unjamming, one or both of its linear elastic moduli becomes very small [22–24]. As a result, its response to a locally imposed shear transformation tends to be nonlinear. To understand the origin of this nonlinearity, consider two contacting grains within the medium. When subjected to a compressive force, the grains remain in contact, whereas a tensile force tends to pull them apart. This asymmetric response is thus more conducive to the propagation of compressive as opposed to tensile stresses. We thus expect the material’s nonlinear response to a localized solicitation to be biased towards isotropic dilation [Fig. 1(c,d)], an effect which we have previously referred to as rectification [25, 26]. Here, we validate this isotropization using numerical simulations of two-dimensional granular packings. We find that the system’s tendency to isotropization diverges as unjamming is approached, in quantitative agreement with predictions from a nonlinear elastic model [26]. Finally we use a toy model to illustrate that in amorphous solids close to unjamming, the yielding transition may as a result display critical exponents and qualitative features different from those predicted in the absence of isotropization.

Stress propagation around a shear transformation near unjamming. We consider packings of frictionless bidisperse disks in a circular arena of radius r_{out} at mechanical equilibrium [details in SI]. The two types of disks are present in equal proportions, the ratio of their diameters is 1.4 and we take the mean diameter as our length unit. The disk area fraction ϕ is set above and close to the critical value $\phi_c \simeq 0.84$ at which the packing unjams [22], such that $\Delta\phi = \phi - \phi_c \lesssim 0.2$. A pair of disks with overlap δ interacts elastically via a Hertzian potential proportional to $\delta^{5/2}$ [27]. The associated stiffness sets our unit of stress. For the values of ϕ considered here, this results in a low initial pressure $P_{\text{init}} \lesssim 0.02$. To mimic stress propagation around a shear transformation, we subject the packings to internal forces at a radius r_{in} [Fig. 2(a)]. In practice, we use mesoscopic values for r_{in} to mitigate the fluctuations due to the medium’s disorder, and apply forces of the order of or smaller than P_{init} to prevent extensive plastic reorganizations [9].

We characterize the magnitude and anisotropy of these forces through the corresponding coarse-grained local stress tensor $\bar{\sigma}^l$ [definition in SI]. We monitor stress propagation via the boundary stress tensor $\bar{\sigma}^b$, which characterizes the forces exerted by the medium at its boundary. Our local forcing is characterized by the two independent components of $\bar{\sigma}^l$: the isotropic pressure \mathcal{P}_l and the shear stress \mathcal{S}_l , respectively illustrated in Figs. 2(b) and (c). We decompose $\bar{\sigma}^b$ similarly. Placing ourselves in the

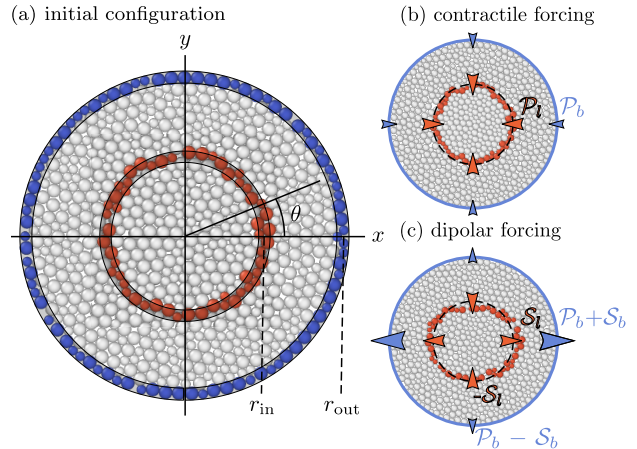


FIG. 2. **We subject circular jammed packings to small internal forces.** (a) Packing of the type used in our simulations but with fewer disks. We exert radial forces on the disks located in the shaded region near r_{in} (orange), and measure the forces exerted on the disks located in the shaded region near r_{out} (blue). (b) The same packing under isotropic contractile forcing, $\mathcal{P}_l < 0$, corresponding to a local shrinkage of the original orange ring. In the final configuration, some gray disks are now subject to the forcing, and some orange ones are not. The dashed circle has radius r_{in} . (c) Dipolar forcing, $\mathcal{S}_l > 0$.

eigenbasis of tensor $\bar{\sigma}^l$, we write

$$\bar{\sigma}^i = - \begin{pmatrix} \mathcal{P}_i + \mathcal{S}_i & 0 \\ 0 & \mathcal{P}_i - \mathcal{S}_i \end{pmatrix} \quad (1)$$

for $i \in \{l, b\}$. Qualitatively, a positive \mathcal{P}_b corresponds to an overall dilation of the medium. Note that for an individual realization of our granular packing, the off-diagonal components of $\bar{\sigma}^b$ in Eq. (1) may not vanish. Symmetry however imposes that their average over the disorder does, and in practice the off-diagonal components do not exceed 10% of the diagonal ones for any of our individual packings.

In the initial configurations, the confining pressure elicits an isotropic array of force chains [Fig. S1]. The application of a dipolar forcing $\mathcal{S}_l > 0$ rearranges the force chains anisotropically as shown in Fig. 3(a). We focus on the outer region $r > r_{\text{in}} + \frac{1}{2}$ through which the local forcing propagates to the boundary. As \mathcal{S}_l increases and nonlinearities become prevalent, the force chains located in the vicinity of the y axis become weaker. In this example, the packing even fractures locally just above and below the orange ring of radius r_{in} . At the same time, the force chains in the vicinity of the x axis are reinforced, both horizontally but also in directions with significant angles with the x axis. At large values of r , this anisotropic propagation leads to the presence of force chains even close to the y axis. As a result an emergent dilational boundary pressure $\mathcal{P}_b > 0$ builds

up in response to the local shear stress \mathcal{S}_l [Figs. 3(b,c) and S3]. In extreme cases, this can rectify boundary stresses toward dilation in all directions, thus making them more isotropic, see Fig. 3(d). Under isotropic forcing $\mathcal{P}_l \neq 0$, we additionally observe nonlinear relationships between \mathcal{P}_b and \mathcal{P}_l [Fig. S4]. Overall, this minimal new setup clearly shows how microscopic force chain rearrangements induce the isotropization of propagated stresses illustrated in Fig. 1.

Dependence of the non-Eshelby propagation on material behavior. To assess the relationship between isotropization and unjamming, we now turn to theory. Within the linear regime, homogeneous elastic media propagate stress without alteration, such that $\mathcal{P}_b = \mathcal{P}_l$ and $\mathcal{S}_b = \mathcal{S}_l$. For weak nonlinearities, symmetries dictate

$$\mathcal{P}_b \sim \mathcal{P}_l + \alpha \mathcal{S}_l^2 + \beta \mathcal{P}_l^2 \quad \text{and} \quad \mathcal{S}_b \propto \mathcal{S}_l. \quad (2)$$

The term $\alpha \mathcal{S}_l^2$, if large and positive, induces dilational stresses that come to dominate the medium's response and is thus responsible for isotropization. In a previous paper [26], we expressed α as a function of the material's elastic properties. To parameterize those, we consider a jammed disk packing initially at $\phi_c + \Delta\phi$ subjected to a small additional compression $\delta\phi \ll \Delta\phi$. To first order in $\delta\phi$, this results in differential bulk and shear moduli that respectively read

$$\kappa = \kappa_0 \left(1 - \kappa_1 \frac{\delta\phi}{\phi_c} \right) \quad \text{and} \quad \mu = \mu_0 \left(1 - \mu_1 \frac{\delta\phi}{\phi_c} \right). \quad (3)$$

The isotropization coefficient α then reads

$$\alpha = -\frac{1}{\mu_0} \left[\left(\kappa_1 + \frac{3}{2} \right) \alpha_1 + \left(\mu_1 + \frac{3}{2} \right) \alpha_2 \right], \quad (4)$$

where α_1 and α_2 are positive functions of the ratio of radii $r_{\text{out}}/r_{\text{in}}$ and Poisson's ratio $\nu = (\kappa_0 - \mu_0)/(\kappa_0 + \mu_0)$ (see SI for full expressions).

For granular materials under Hertzian interactions, the bulk and shear moduli vanish at unjamming as $\kappa \sim \kappa_0 \approx \sqrt{\Delta\phi}$ and $\mu \sim \mu_0 \approx \Delta\phi$ [22, 28]. The resulting relative insignificance of the shear modulus $\mu/\kappa \approx \sqrt{\Delta\phi}$ for small $\Delta\phi$ hints that nonlinear effects such as isotropization could become prominent near unjamming. Expanding these expressions for small $\delta\phi$ and equating the result to Eq. (3) yields

$$\kappa_1 \underset{\Delta\phi \rightarrow 0}{\sim} -\frac{1}{2} \frac{\phi_c}{\Delta\phi} \quad \text{and} \quad \mu_1 \underset{\Delta\phi \rightarrow 0}{\sim} -\frac{\phi_c}{\Delta\phi}. \quad (5)$$

Therefore, κ_1 and μ_1 are both negative. Granular media indeed soften under tension ($\delta\phi < 0$) and stiffen under compression. These nonlinear coefficients moreover diverge near unjamming as $(\Delta\phi)^{-1}$, leading to a large positive isotropization coefficient α [SI]. According to Eq. (2), an anisotropic forcing already gives rise to a significantly

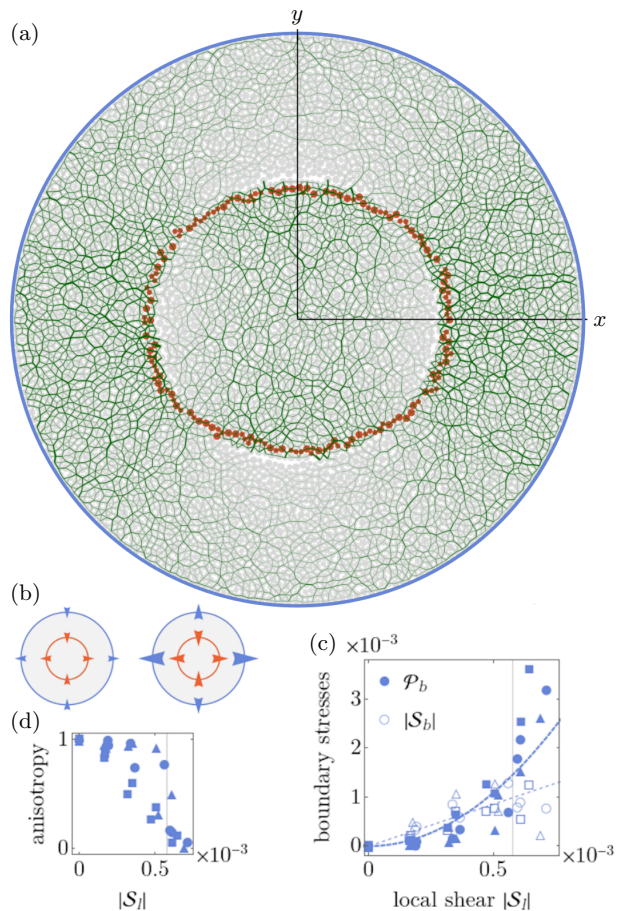


FIG. 3. Force chains rearrange to create boundary dilation out of local shear stress. (a) Local shear stress induces anisotropic force chains in a packing. The green segments have widths proportional to the forces between neighboring disks. We refer to consecutive segments with large widths as force chains. Here we have $\simeq 6700$ disks, $r_{\text{out}} \simeq 44$, $r_{\text{out}}/r_{\text{in}} = 2$, $\Delta\phi \simeq 0.03$. (b) Illustration of the corresponding local and boundary coarse-grained stresses. (c) Dilation under dipolar forcing for three initial configurations (circles, squares and triangles), demonstrating reproducibility. We fit the data using $\mathcal{P}_b = \alpha \mathcal{S}_l^2$ with $\alpha \simeq 4400$, and $\mathcal{S}_b = (1 + B)\mathcal{S}_l$ with $B \simeq 0.7$. Here $r_{\text{out}}/r_{\text{in}} = 8$, $r_{\text{in}} \simeq 5.5$, $\Delta\phi \simeq 0.03$. (d) The boundary stress anisotropy $\mathcal{S}_b^2/(\mathcal{S}_b^2 + \mathcal{P}_b^2)$ decreases as the local shear stress increases. The vertical line indicates the local shear stress at which this anisotropy falls under $\frac{1}{2}$.

isotropized far-field boundary stress (*i.e.*, $\mathcal{P}_b > \mathcal{S}_b$) for a small $\mathcal{S}_l \approx \alpha^{-1} \approx (\Delta\phi)^2$.

To confirm this predominance of isotropization in the vicinity of unjamming, we measure coefficients α and β in simulations of the type of those presented in Fig. 3 for different values of $\Delta\phi$ and r_{in} (additional fits in Figs. S3-S5) and report them in Fig. 4. We find that the small-nonlinearity expansion of Eq. (2) describes our data well even in regimes where the nonlinear terms are

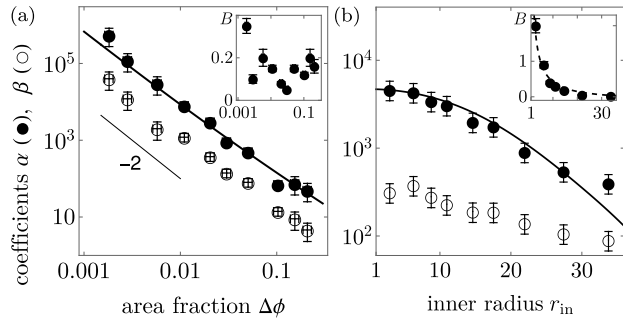


FIG. 4. **Isotropization prevails close to jamming and in large systems.** (a) Log-log plot of coefficients α and β obtained as in the fits of Fig. 3(c) showing a $(\Delta\phi)^{-2}$ divergence as unjamming is approached. The black line shows our theoretical predictions [Eq. (4)] and we observe $\beta \simeq \alpha/9$. *Inset:* the phenomenological coefficient B does not strongly depend on $\Delta\phi$. Here $r_{\text{in}} \simeq 5.5$ and $r_{\text{out}} \simeq 44$. (b) Holding the outer radius $r_{\text{out}} \simeq 44$ constant, the isotropization coefficient α is strongest for small r_{in} , in agreement with the theoretical prediction (SI). *Inset:* B is also large for small r_{in} ; the dashed line shows a heuristic dependence $B = (r_{\text{out}}/r_{\text{in}} - 1)/8$. Here $\Delta\phi \simeq 0.03$. Bars show standard deviation across three simulations.

comparable to or larger than the linear ones. We observe an unexpected steeper linear dependence $S_b = (1 + B)S_l$ than predicted, but find that the phenomenological coefficient $B > 0$ is not large enough to prevent isotropic dilation from dominating the response of our packings (insets of Fig. 4). Both coefficients α and β are positive, and thus contribute to the medium's dilation in the nonlinear regime. This dilation is moreover strongest for small $\Delta\phi$ and for a very localized forcing (r_{in} small). Finally, we compare the values of the main isotropization coefficient α to the prediction of Eqs. (4-5). We find a very good agreement without any adjustable parameters (we obtain κ_0 and μ_0 from Refs. [22, 28]), confirming that close to unjamming, the weakening of the packing's linear response induces an overwhelmingly dilational, non-Eshelby response to localized forces.

Macroscopic implications of the non-Eshelby propagator. In amorphous solids, shear transformations tend to induce further local plastic reorganizations through stress propagation. In elasto-plastic models, the characteristics of the resulting yielding transition rely on the quadrupolar symmetry of the Eshelby propagator. Due to this symmetry, a shear transformation is equally likely to drive any neighboring region towards or away from a plastic reorganization. Loosely defining a scalar stress σ characterizing how far the region is from the reorganization threshold σ_c , this implies that σ undergoes a symmetric random walk prior to reaching σ_c . By contrast, Eq. (2) predicts an additional dilational stress \mathcal{P}_b , which should bias the random walk and change some universal

characteristics of the system's fluidization transition.

To illustrate the macroscopic implications of this breaking of the stress-reversal symmetry, we turn to a simple mean-field elasto-plastic model [4]. The model monitors the temporal evolution of the probability density $P(\sigma, t)$ for a region of the amorphous solid to have a local stress σ at time t . In a material under external shear at a rate $\dot{\gamma}$, σ systematically increases at rate $\mu\dot{\gamma}$. It also diffuses via the random positive and negative stress increments resulting from shear transformations in the rest of the material. The associated diffusion coefficient $D = a\Gamma$ is proportional to the number Γ of plastic reorganizations per unit time. To account for the dilational bias \mathcal{P}_b away from yielding we introduce an additional drift term $-bD$ to the evolution equation for $P(\sigma, t)$, where a and b are both constants:

$$\partial_t P = -(\mu\dot{\gamma} - ba\Gamma)\partial_\sigma P + a\Gamma\partial_\sigma^2 P - \nu(\sigma)P + \Gamma\delta(\sigma). \quad (6)$$

Here, the disappearance rate $\nu(\sigma) = \tau^{-1}H(|\sigma| - \sigma_c)$, where H denotes the Heaviside step function, implies that each region whose stress exceeds the critical value σ_c undergoes a plastic reorganization and is removed from the system. It is then reintroduced as a new stressless configuration through the last term of Eq. (6) involving Dirac's delta function δ , with the condition that $\Gamma(t) = \int_{-\infty}^{+\infty} \nu(\sigma)P(\sigma, t) d\sigma$. As b quantifies the relative importance of the dilational and Eshelby stress propagation, we expect it to become relevant close to unjamming.

Analyzing Eq. (6) in a steady state [details in SI] reveals that just like the classical $b = 0$ case, our extended $b \neq 0$ model displays an unjamming transition from a solid-like phase devoid of plastic events at zero shear rate ($\Gamma = 0$) to a fluid-like phase ($\Gamma \neq 0$) upon an increase of a through a critical value. At the transition, the rheology of the material is described by a Herschel-Bulkley exponent of $1/2$:

$$\langle\sigma\rangle - \langle\sigma(\dot{\gamma} = 0)\rangle \approx \dot{\gamma}^{1/2}. \quad (7)$$

By contrast, in the Eshelby-like ($b = 0$) case this dependence is $\langle\sigma\rangle \approx \dot{\gamma}^{1/5}$ and only crosses over to a Herschel-Bulkley exponent of $1/2$ deeper in the jammed phase [29]. While derived in a simplistic model, this indicates that the loss of the Eshelby-like symmetry can have macroscopic implications for the rheology of amorphous materials.

Discussion. Our study sheds light on the transmission of internally generated stresses in granular systems close to unjamming. Many elasto-plastic models are predicated on the assumption that following a shear transformation, this transmission is well described by an Eshelby-like linear elasticity kernel [1, 6, 30]. We show that elastic nonlinearities inherent to the unjamming transition instead lead to substantial isotropic dilational stresses around local rearrangements. This isotropization is strongest

for rearrangements with sizes of a few particle diameters, comparable to that of shear transformations [31]. This mirrors earlier experimental [17] and numerical [21] findings.

While our analysis is focused on packings of disks with Hertzian interactions, we expect similar results for harmonic interactions [SI] and random spring networks [32, 33]. This universal character is reflected in the good agreement between our simulations and a continuum theory devoid of specific microscopic assumptions. While based on a small-stress, weakly nonlinear expansion, this formalism quantitatively predicts isotropized stresses even in regimes where they are significantly larger than the stresses predicted by linear elasticity. This is reminiscent of successful predictions of the onset of failure in amorphous solids based on lowest-order nonlinearities [34]. Beyond this robustness to specific material properties, our prediction of large isotropization at unjamming crucially relies on the vanishing of at least one elastic modulus at this transition. Systems where K and G remain finite at the transition should thus display negligible far-field stress isotropization.

We use an elasto-plastic toy model to bring out the macroscopic consequences of the isotropization-induced breaking of the symmetry between positive and negative stresses. Consistent with recent non-mean-field results, we find that breaking this symmetry changes the characteristics of the unjamming transition [35]. Moreover, yielding in strongly jammed systems where this symmetry is present tends to concentrate along transient slip lines [13, 36, 37]. We thus predict more homogeneous, ductile-like yielding patterns in weakly-jammed systems due to more isotropic propagated stresses [14, 38].

Acknowledgments. ML and FB thank Éric Clément and Sylvain Patinet for fruitful discussions. ML was supported by Marie Curie Integration Grant PCIG12-GA-2012-334053, “Investissements d’Avenir” LabEx PALM (ANR-10-LABX-0039-PALM), ANR-21-CE11-0004-02, ANR-22-ERCC-0004-01 and ANR-22-CE30-0024-01, as well as ERC Starting Grant 677532 and the Impulscience program of Fondation Bettencourt-Schueller. ML’s group belong to the CNRS consortium AQV.

* fbenoit@igc.gulbenkian.pt

† martin.lenz@universite-paris-saclay.fr

- [1] A. Nicolas, E. E. Ferrero, K. Martens, and J.-L. Barrat, *Rev. Mod. Phys.* **90**, 045006 (2018).
- [2] D. Bonn, M. M. Denn, L. Berthier, T. Divoux, and S. Manneville, *Rev. Mod. Phys.* **89**, 035005 (2017).
- [3] A. Argon, *Acta Metall.* **27**, 47 (1979).
- [4] P. Hébraud and F. Lequeux, *Phys. Rev. Lett.* **81**, 2934 (1998).
- [5] L. Bocquet, A. Colin, and A. Ajdari, *Phys. Rev. Lett.* **103**, 036001 (2009).
- [6] J. Lin, E. Lerner, A. Rosso, and M. Wyart, *Proc. Natl. Acad. Sci. U.S.A.* **111**, 14382 (2014).
- [7] Z. Budrikis, D. F. Castellanos, S. Sandfeld, M. Zaiser, and S. Zapperi, *Nat. Commun.* **8**, 15928 (2017).
- [8] M. Talamali, V. Petäjä, D. Vandembroucq, and S. Roux, *Phys. Rev. E* **84**, 016115 (2011).
- [9] M. Bouzid, A. Izzet, M. Trulsson, E. Clément, P. Claudin, and B. Andreotti, *Eur. Phys. J. E* **38**, 125 (2015).
- [10] J. D. Eshelby, *Proc. R. Soc. A: Math. Phys. Eng. Sci.* **241**, 376 (1957).
- [11] K. Karimi and J.-L. Barrat, *Sci. Rep.* **8**, 4021 (2018).
- [12] J. Lin, A. Saade, E. Lerner, A. Rosso, and M. Wyart, *Europhys. Lett.* **105**, 26003 (2014).
- [13] R. Dasgupta, H. G. E. Hentschel, and I. Procaccia, *Phys. Rev. Lett.* **109**, 255502 (2012).
- [14] B. Tyukodi, S. Patinet, S. Roux, and D. Vandembroucq, *Phys. Rev. E* **93**, 063005 (2016).
- [15] K. Martens, L. Bocquet, and J.-L. Barrat, *Soft Matter* **8**, 4197 (2012).
- [16] A. Kabla and G. Debrégeas, *Phys. Rev. Lett.* **90**, 258303 (2003).
- [17] K. W. Desmond and E. R. Weeks, *Phys. Rev. Lett.* **115**, 098302 (2015).
- [18] A. Tanguy, F. Leonforte, and J.-L. Barrat, *Eur. Phys. J. E* **20**, 355 (2006).
- [19] A. J. Liu and S. R. Nagel, *Nature* **396**, 21 (1998).
- [20] M. van Hecke, *J. Phys.: Condens. Matter* **22**, 033101 (2009).
- [21] J. A. Giannini, E. Lerner, F. Zamponi, and M. L. Manning, *J. Chem. Phys.* **160**, 034502 (2024).
- [22] C. S. O’Hern, L. E. Silbert, A. J. Liu, and S. R. Nagel, *Phys. Rev. E* **68**, 011306 (2003).
- [23] S. Dagois-Bohy, E. Somfai, B. P. Tighe, and M. van Hecke, *Soft Matter* **13**, 9036 (2017).
- [24] M. S. van Deen, J. Simon, Z. Zeravcic, S. Dagois-Bohy, B. P. Tighe, and M. van Hecke, *Phys. Rev. E* **90**, 020202 (2014).
- [25] P. Ronceray, C. P. Broedersz, and M. Lenz, *Proc. Natl. Acad. Sci. U.S.A.* **113**, 2827 (2016).
- [26] F. Benoist, G. Saggiorato, and M. Lenz, *Soft Matter* **19**, 2970 (2023).
- [27] H. A. Makse, N. Gland, D. L. Johnson, and L. M. Schwartz, *Phys. Rev. E* **70**, 061302 (2004).
- [28] C. Zhao, K. Tian, and N. Xu, *Phys. Rev. Lett.* **106**, 125503 (2011).
- [29] E. Agoritsas, E. Bertin, K. Martens, and J.-L. Barrat, *Eur. Phys. J. E* **38**, 71 (2015).
- [30] S. Merabia and F. Detcheverry, *Europhys. Lett.* **116**, 46003 (2016).
- [31] A. Amon, V. B. Nguyen, A. Bruand, J. Crassous, and E. Clément, *Phys. Rev. Lett.* **108**, 135502 (2012).
- [32] E. Lerner, E. DeGiuli, G. Düring, and M. Wyart, *Soft Matter* **10**, 5085 (2014).
- [33] W. Ellenbroek, Z. Zeravcic, W. Saarloos, and M. van Hecke, *Europhys. Lett.* **87**, 34004 (2009).
- [34] S. Karmakar, A. Lemaître, E. Lerner, and I. Procaccia, *Phys. Rev. Lett.* **104**, 215502 (2010).
- [35] T. Jocteur, S. Figueiredo, K. Martens, E. Bertin, and R. Mari, *Phys. Rev. Lett.* **132**, 268203 (2024).
- [36] C. E. Maloney and A. Lemaître, *Phys. Rev. Lett.* **93**, 016001 (2004).
- [37] C. E. Maloney and A. Lemaître, *Phys. Rev. E* **74**, 016118 (2006).

[38] D. Richard *et al.*, [Phys. Rev. Mater.](#) **4**, 113609 (2020).

Supporting information for “Stress Isotropization in Weakly Jammed Granular Packings”

I. GRANULAR DYNAMICS SIMULATIONS

Here, we give details on the mechanical analyses of randomly-jammed disk packings in a circular arena. We describe the process to obtain equilibrated circular packings in Sec. **IA**. These correspond to initial configurations that we then gently perturb with a circular active unit. We precisely define the local and boundary coarse-grained stress tensors. We go on to discuss their expected behaviors at intermediate forcing in Sec. **IB**. In Sec. **IC**, we then present additional results under isotropic forcing and in additional parameter regimes. Finally, we describe in Sec. **ID** the expulsion of the disks at high forcing.

A. Equilibrium jammed configurations gently perturbed

We consider randomly-jammed disk packings inside a circular arena. From an initial unjammed configuration at low density, we increase the disk diameters until a jammed configuration at a given target density ϕ is obtained. But this configuration is obviously out of equilibrium, such that any posterior change on the system will dramatically change its properties. To reach a more stable configuration, we let the system slowly relax by thermal agitation using a granular dynamics algorithm via the software LAMMPS [1] version stable.23Jun2022. In this procedure, the temperature T is slowly decreased to reach a more stable local equilibrium [2–4]. If the initial compression is not large enough, such that the target $\phi < \phi_c$, then a jammed packing with nonzero pressure cannot be obtained which helps determining the particular value of ϕ_c for a given packing history. We then determine $\Delta\phi = \phi - \phi_c$ precisely for each packing via the values of the initial pressure (after equilibration) $P_{\text{init}} \sim (\Delta\phi)^{3/2}$ and excess contact number $Z_{\text{init}} - 4 \sim \sqrt{\Delta\phi}$ compared to the isostatic ($Z = 4$) case. Given the largest interpenetration $P_{\text{init}}/k \simeq 2\%$, the average distance between two disks in contact is roughly the mean disk diameter D . We use 50:50 bidisperse disks with a ratio of diameters 1.4 to prevent triangular arrangements, such that the configurations are random [5, 6]. This yields initial configurations with isotropic force chains as displayed in Fig. **S1**.

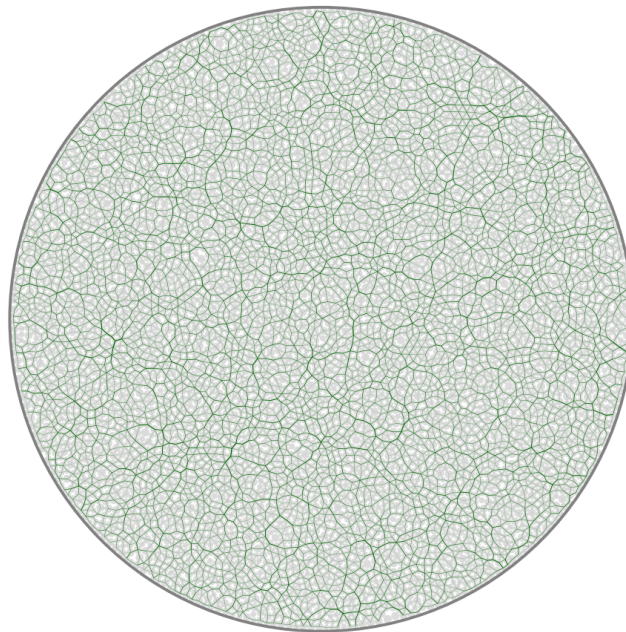


FIG. S1. **Isotropic force chains in an initial configuration.** Fig. 3(a) corresponds to the same realization under forcing.

Interaction details. Both inter-disk and disk-arena interactions are modeled as Hertzian, with normal elastic and viscous stiffnesses $k = 1000$ in pressure units and $\gamma = 73$ in inverse units of time. We set the friction coefficient to zero, which suppresses any tangential forces. The choice of γ corresponds to a particle mass $\frac{\pi}{6}$ and a coefficient of restitution $e_r = 0.1$. Given the contact time $\tau_c = \frac{2}{\gamma} \ln e_r$, we set the time interval $dt = \tau_c/50 \simeq 5.5 \times 10^{-4}$ such that the dynamics is realistic [7]. The precise values of k, γ and e_r do not matter for the equilibrated values of P/k and Z .

Equilibration protocol. We initialize a gas of disks with equal mass within a circular arena. The positions are taken uniformly at random and the speeds follow a Maxwellian distribution with temperature T . A seed is used for the positions and the velocities, so that we can study the packings with similar histories and thus similar critical area fractions ϕ_c . We increase the radii of the big and small disks with the same rate until the desired ϕ is reached. We then let the grains equilibrate in three consecutive stages at decreasing temperatures: $T/k = 10^{-7}$, 10^{-9} and 10^{-11} , and measure the pressure P/k and the contact number Z along the way, where k is the elastic stiffness. The sudden jumps in T help ensuring that a quasi-stable equilibrium is reached, and resolve technical issues with the calculations of physical observables. Below ϕ_c the pressure goes to very low values ($\simeq 10^{-8}$) and decreases with the temperature jumps [6]. But above ϕ_c , once a local potential energy minimum is reached, the pressure goes to a value independent of T . We declare that a configuration is equilibrated when 5×10^5 simulation steps give similar values.

Local forcing and coarse-grained stresses. To analyze the packing response to a local forcing, we define an inner annular region inside the arena such that $r \in I_l = [r_{\text{in}} - \frac{D}{2}, r_{\text{in}} + \frac{D}{2}]$ (orange disks in Fig. 2(a)). In addition to the forces due to the initial pressure P_{init} , we add a small constant component to the radial force of each disk μ in the inner ring:

$$\mathbf{f}^\mu/k = (f_0 + 2f_2 \cos 2\theta^\mu) \hat{\mathbf{r}}^\mu, \quad \text{for } r^\mu \in I_l, \quad (\text{S1})$$

where f_0, f_2 refer to the isotropic and dipolar parts. We further consider two types of forcing: isotropic when $f_2 = 0$ [Fig. 2(b)], and dipolar when $f_0 = 0$ [Fig. 2(c)]. The forcing of Eq. (S1) elicits a coarse-grained local stress proportional to the dipole of the added forces:

$$\bar{\sigma}_{ij}^l = \frac{-2D}{kA_l} \sum_{\mu \in I_l} f_i^\mu \hat{r}_j^\mu, \quad (\text{S2})$$

where the area of the inner ring $A_l = 2\pi r_{\text{in}} D$. We likewise define a boundary ring $r \in I_b = [r_{\text{out}} - \frac{D}{2}, r_{\text{out}} + \frac{D}{2}]$ (blue disks in Fig. 2(a)), whose outer part sticks to the arena. By measuring the elastic stress tensor on each disk in the boundary ring, σ^μ (in units of stress times area), relative to the one in the initial configuration without added force, $\sigma^{\mu, f=0}$, we can compute the coarse-grained boundary stress

$$\bar{\sigma}_{ij}^b = \frac{2}{kA_b} \frac{r_{\text{out}}^2}{r_{\text{in}}^2} \sum_{\mu \in I_b} (\sigma_{ik}^\mu - \sigma_{ik}^{\mu, f=0}) \hat{r}_k^\mu \hat{r}_j^\mu, \quad (\text{S3})$$

which represents the macroscopic stress response of the packing. Here the area of the boundary ring $A_b = 2\pi r_{\text{out}} D$, the summation on repeated indices is implied, and the ratio $r_{\text{out}}^2/r_{\text{in}}^2$ compensates for the dilution, such that the analytical predictions in linear elastic systems correspond to $\bar{\sigma}^b = \bar{\sigma}^l$ [8]. Using the definitions of $\mathcal{P}_l, \mathcal{P}_b, \mathcal{S}_l$ and \mathcal{S}_b in the main text, we find that up to the intermediate force regime where $f_0, f_2 \lesssim P_{\text{init}}/k$, the local stresses increase linearly with the force components as $\mathcal{P}_l \propto f_0$ and $\mathcal{S}_l \propto f_2$.

B. Data convergence at intermediate forcing

Under forcing, we let the system relax until the data converge to a roughly constant value, see Fig. S2. In the isotropic case ($f_2 = 0$), since the forces are applied on all disks in the local ring at each time step, two distinct regions appear. For a contractile active unit $f_0 < 0$, the inner region has a higher contact number, while the outer region has a lower one. Whereas flows tend to appear in the dipolar case ($f_0 = 0$). In Fig. 3(c,d) for instance, the flows stop before data acquisition up to $\mathcal{S}_l \simeq 6 \times 10^{-4}$, while they do not stop for higher values of \mathcal{S}_l . Surprisingly the presence of non-stopping flows, which clearly disrupt the packing history by producing irreversible rearrangements all over the system, has no visible effect on the data.

The elastic stress on each disk μ depends on the the positions of its neighbors $\{\mathbf{r}^\nu\}$ and the forces that they exert $\{f^{\nu \rightarrow \mu}\}$ as

$$\sigma_{ij}^\mu = - \sum_{\nu \text{ neigh.}} (r_i^\nu - r_i^\mu) f_j^{\mu \rightarrow \nu}. \quad (\text{S4})$$

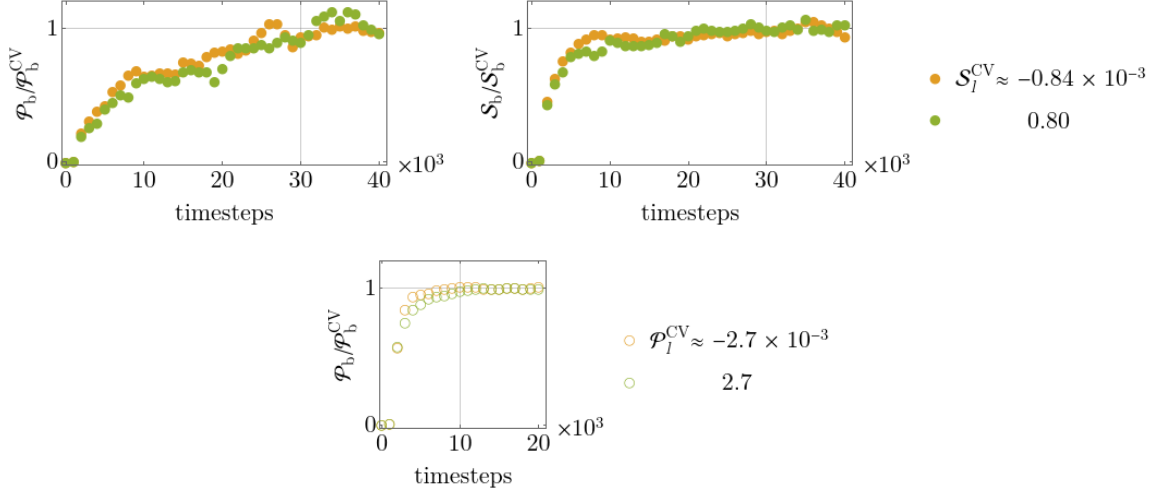


FIG. S2. **Typical time series show an approximate convergence.** Same settings as in Fig. 3(c,d). At $\Delta\phi \simeq 0.03$, the converged values $\mathcal{P}_b^{\text{CV}}, \mathcal{S}_b^{\text{CV}}$ are averaged between 3 and 4×10^4 steps in the dipolar case, and between 1 and 2×10^4 in the isotropic case. Filled (empty) symbols refer to dipolar (isotropic) forcing.

This explains why we can relate σ^μ in Eq. (S3) to the term $-D\mathbf{f}^\mu$ in Eq. (S2). Moreover, we can recover the equations $\mathcal{P}_l \propto f_0$ and $\mathcal{S}_l \propto f_2$ by approximating the sum in the definition of the local coarse-grained stress as an integral:

$$\bar{\sigma}_{ij}^l \approx \frac{-2D}{kA_l} N_l \int_0^{2\pi} \frac{d\theta}{2\pi} f_i \hat{r}_j, \quad (\text{S5})$$

where $\hat{r}_j = \delta_{jx} \cos\theta + \delta_{jy} \sin\theta$ and N_l stands for the number of disks in the inner ring. Then from Eq. (S2), we obtain

$$\mathcal{P}_l = -\frac{\bar{\sigma}_{xx}^l + \bar{\sigma}_{yy}^l}{2} \approx \frac{D}{A_l} N_l \int_0^{2\pi} \frac{d\theta}{2\pi} (f_0 + 2f_2 \cos 2\theta)(\cos^2\theta + \sin^2\theta) \approx \frac{DN_l}{A_l} f_0, \quad (\text{S6a})$$

$$\mathcal{S}_l = -\frac{\bar{\sigma}_{xx}^l - \bar{\sigma}_{yy}^l}{2} \approx \frac{D}{A_l} N_l \int_0^{2\pi} \frac{d\theta}{2\pi} (f_0 + 2f_2 \cos 2\theta)(\cos^2\theta - \sin^2\theta) \approx \frac{DN_l}{A_l} f_2. \quad (\text{S6b})$$

We now focus on the definition of the boundary stress in Eq. (S3). There, the ratio of radii squared in $\bar{\sigma}^b$ compensates for the dilution of the local stress $\bar{\sigma}^l$ over the system area as the radius increases from r_{in} to r_{out} . Approximating the stress on the disks as a continuum stress field in polar coordinates and introducing $\Delta\sigma = \sigma - \sigma^{f=0}$, we can write

$$\mathcal{P}_b \approx -\frac{N_b}{A_b} \frac{r_{\text{out}}^2}{r_{\text{in}}^2} \int_0^{2\pi} \frac{d\theta}{2\pi} \frac{\Delta\sigma_{rr}(r_{\text{out}}, \theta)}{k}, \quad (\text{S7a})$$

$$\mathcal{S}_b \approx -\frac{N_b}{A_b} \frac{r_{\text{out}}^2}{r_{\text{in}}^2} \int_0^{2\pi} \frac{d\theta}{2\pi} \frac{\Delta\sigma_{rr}(r_{\text{out}}, \theta) \cos 2\theta - \Delta\sigma_{\theta r}(r_{\text{out}}, \theta) \sin 2\theta}{k}, \quad (\text{S7b})$$

where N_b stands for the number of disks in the boundary ring. Therefore, by decomposing the stress field as

$$\Delta\sigma(r, \theta) = \mathbf{a}^{(0)}(r) + \sum_{n>0} \mathbf{a}^{(n)}(r) \cos n\theta + \mathbf{b}^{(n)}(r) \sin n\theta, \quad (\text{S8})$$

we see that only the term $a_{rr}^{(0)}$ contributes to \mathcal{P}_b . Whereas, only the terms $a_{rr}^{(2)}$ and $b_{\theta r}^{(2)}$ contribute to \mathcal{S}_b , in correspondence with the dependencies of the local stresses: $\mathcal{P}_l \propto f_0$ and $\mathcal{S}_l \propto f_2$.

C. Additional data at intermediate forcing

Here, Fig. S3 displays additional results under dipolar forcing. The lower system size compared to the case of Fig. 3(c,d) yields an expected weaker isotropization. We then show results of simulations under isotropic forcing in

Fig. S4. Finally, Fig. S5 shows results under dipolar plus isotropic forcing. All data are shown for different packing histories and appear quite reproducible.

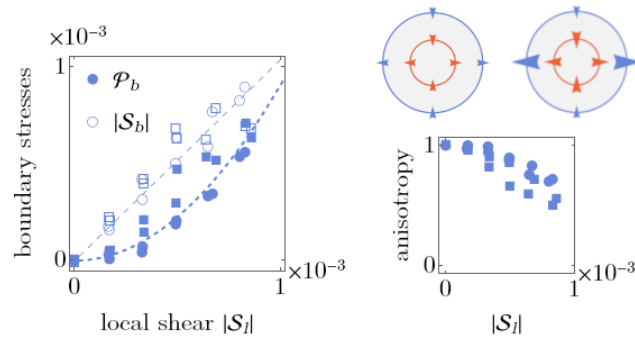


FIG. S3. **Weaker isotropization under dipolar forcing** for $r_{\text{out}}/r_{\text{in}} = 2$. Other settings as in Fig. 3(c,d). The fits give $\alpha \simeq 910$ and $B \simeq 0.04$. Here, the vertical boundary stress $\mathcal{P}_b - |\mathcal{S}_b|$ remains contractile (negative) in the intermediate forcing regime.

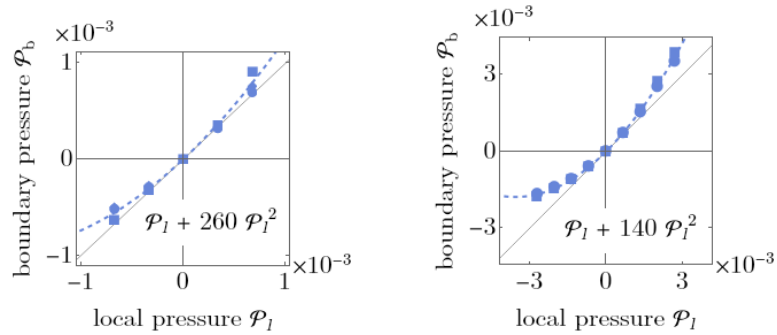


FIG. S4. **Dilational tendency under isotropic forcing.** The quadratic fit gives $\beta \simeq 260$ when $r_{\text{out}}/r_{\text{in}} = 8$, and $\beta \simeq 140$ when $r_{\text{out}}/r_{\text{in}} = 2$. Other settings as in Fig. 3(c,d).

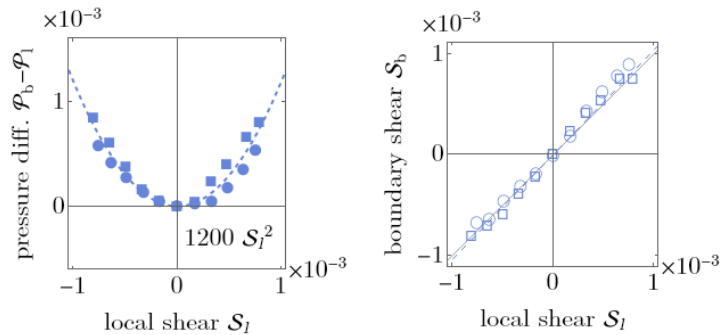


FIG. S5. **The dilation effects add up under dipolar plus isotropic forcing.** Same settings as in Fig. 3(c,d) except that $r_{\text{out}}/r_{\text{in}} = 2$. Here, $f_0 = f_2$ leads to $\mathcal{P}_l \approx \mathcal{S}_l$. The total coefficient 1200 roughly corresponds to the sum of the coefficients under dipolar and isotropic forcing of Figs. S3 and S4 respectively: $910 + 140 = 1150$.

D. Expulsion of the disks at high forcing

At high forcing $f_0, f_2 \gtrsim P_{\text{init}}/k$, Fig. S6 shows how the number of disks in the local ring N_l falls below 70% of its initial value. This causes the coarse-grained stresses to saturate, such that the local stress components no longer obey the relationships $\mathcal{P}_l \propto f_0$ and $\mathcal{S}_l \propto f_2$.

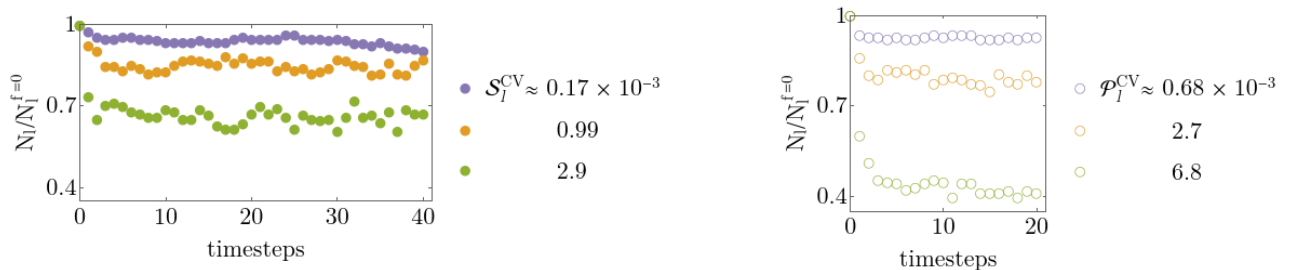


FIG. S6. **The disks are expelled from the local ring at high forcing.** This is shown by the relative decrease in the number of disks in the local ring N_l compared to the situation without forcing $N_l^{f=0}$. Filled (empty) symbols refer to dipolar (isotropic) forcing.

II. CONTINUUM ELASTIC MODEL FOR WEAKLY JAMMED GRANULAR MEDIA

In a continuum elastic medium, we previously performed a generic expansion of Hooke's law to the lowest nonlinear order [8]. In two dimensions and under the assumptions of isotropy and achirality, we showed that it leads to two new parameters κ_1, μ_1 corresponding to nonlinear corrections to the bulk and shear moduli κ, μ . We hereby detail the calculation of these parameters in granular media, which can then be plugged in the theoretical expression for the isotropization coefficient α to obtain the curves in Fig. 4 of the main text.

We quantify the elastic deformation of our medium at location \mathbf{x} using the displacement gradient $\eta_{ij} = \partial u_i / \partial x_j$. For small strains $\eta \ll 1$, at the lowest nonlinear order, the Cauchy stress $\boldsymbol{\sigma}$ can be written as a quadratic function of the displacement gradient: $\sigma_{ij} = \mathcal{K}_{ijkl} \eta_{kl} + \mathcal{L}_{ijklmn} \eta_{kl} \eta_{mn} + \mathcal{O}(\eta^3)$ where the summation on repeated indices is implied. In an isotropic and achiral medium under a combination of bulk deformation and simple shear

$$\boldsymbol{\eta} = \begin{pmatrix} \eta_{ii}/2 & \eta_{xy} \\ 0 & \eta_{ii}/2 \end{pmatrix}, \quad (\text{S9})$$

the stress response can be characterized by its differential bulk and shear moduli as

$$\kappa = \frac{\partial \sigma_{xx}}{\partial \eta_{ii}} = \kappa_0 (1 + \kappa_1 \eta_{ii}) + \mathcal{O}(\eta^2), \quad (\text{S10a})$$

$$\mu = \frac{\partial \sigma_{xy}}{\partial \eta_{xy}} = \mu_0 (1 + \mu_1 \eta_{ii}) + \mathcal{O}(\eta^2), \quad (\text{S10b})$$

The right-hand sides of these equations contains all terms up to order 2 which respect the deformation symmetries.

Hertzian interactions. In the setup of Fig. 2, we consider a large 2D packing of frictionless spherical grains with area fraction $\phi_c + \Delta\phi$ interacting through a Hertzian potential $\mathcal{V} \sim k \delta^{5/2}$, where k is the spring constant used in the simulations and δ the overlap divided by the sum of the two disk diameters. For area fractions slightly above the unjamming transition, *i.e.* $0 < \Delta\phi \ll 1$, the bulk and shear moduli can be expressed at the lowest order as [5]

$$\kappa/k = K(\Delta\phi)^s [1 + \mathcal{O}(\Delta\phi)] \quad \text{and} \quad \mu/k = M(\Delta\phi)^t [1 + \mathcal{O}(\Delta\phi)], \quad (\text{S11})$$

where $K \simeq 0.3$, $s \simeq 0.5$, $M \simeq 0.2$ and $t \simeq 1.0$. The area fraction $\phi_c + \Delta\phi$ corresponds to that of a system initially at the rigidity threshold ϕ_c subjected to a small isotropic compression with a bulk strain $\eta_{ii} = -\eta_0$, where $0 < \eta_0 \ll 1$ such that $\eta_0 = \Delta\phi/\phi_c + \mathcal{O}(\Delta\phi)$. We then add an even smaller perturbation to the bulk strain $\eta_{ii} = -\eta_0 - \delta\eta$, where $|\delta\eta| \ll \eta_0$. This $\delta\eta$ thus relates to the $\delta\phi$ in the main text as $\delta\eta = \delta\phi/\phi_c + \mathcal{O}(\Delta\phi)$. This results in elastic moduli

$$\kappa = \kappa_0(1 - \kappa_1 \delta\eta) + \mathcal{O}(\delta\eta^2) \quad \text{and} \quad \mu = \mu_0(1 - \mu_1 \delta\eta) + \mathcal{O}(\delta\eta^2), \quad (\text{S12})$$

where the elastic parameters read

$$\begin{aligned}\kappa_0/k &= K(\Delta\phi)^s [1 + \mathcal{O}(\Delta\phi)], & \kappa_1 &= -\frac{s\phi_c}{\Delta\phi} [1 + \mathcal{O}(\Delta\phi)], \\ \mu_0/k &= M(\Delta\phi)^t [1 + \mathcal{O}(\Delta\phi)], & \mu_1 &= -\frac{t\phi_c}{\Delta\phi} [1 + \mathcal{O}(\Delta\phi)].\end{aligned}\tag{S13}$$

Therefore, around *e.g.* $\Delta\phi = 0.1, 0.01$ or 0.001 , given $\phi_c \simeq 0.84$, we find respectively $\kappa_1 \simeq -4, -40$ or -400 , and $\mu_1 \simeq -8, -80$ or -800 . Poisson's ratio then reads

$$\nu = \frac{\kappa_0 - \mu_0}{\kappa_0 + \mu_0} = 1 - 2\frac{M}{K}(\Delta\phi)^{t-s} [1 + \mathcal{O}(\Delta\phi)].\tag{S14}$$

$1 - \nu$ thus scales approximately as $(\Delta\phi)^{0.5}$, such that media far from unjamming are more compressible. Eqs. (S12) and (S13) thus give a proper meaning to Eqs. (3) and (5) of the main text.

Now that the elastic parameters are properly defined, we input them into the expression of α from [8]. In the continuum approach, $\alpha\mu_0/k$ is a dimensionless function of the ratio of radii $\rho = (r_{\text{out}}/r_{\text{in}})^2$, Poisson's ratio ν , and the corrections to the moduli κ_1 and μ_1 . We introduce three functions of ρ and ν only:

$$\begin{aligned}X &= 4\rho(3 - \nu)^2 [2(3 + \nu) + (3 - \nu)(\rho + \rho^2)]^2 / (\rho - 1), \\ \frac{X\alpha_1}{1 - \nu^2} &= 405 - 108\nu - 54\nu^2 + 12\nu^3 + \nu^4 + (324 - 180\nu - 24\nu^2 - 36\nu^3 - 4\nu^4)\rho \\ &\quad + (378 - 288\nu + 120\nu^2 + 24\nu^3 + 6\nu^4)\rho^2 + (108 - 180\nu + 48\nu^2 + 12\nu^3 - 4\nu^4)\rho^3 \\ &\quad + (81 - 108\nu + 54\nu^2 - 12\nu^3 + \nu^4)\rho^4, \\ X\alpha_2 &= 81 - 54\nu + 351\nu^2 - 84\nu^3 - 49\nu^4 + 10\nu^5 + \nu^6 \\ &\quad - (684\nu - 204\nu^2 + 120\nu^3 + 8\nu^4 + 28\nu^5 + 4\nu^6)\rho \\ &\quad + (594 - 900\nu + 1122\nu^2 - 360\nu^3 + 102\nu^4 + 12\nu^5 + 6\nu^6)\rho^2 \\ &\quad + (216 - 1116\nu + 924\nu^2 - 312\nu^3 + 16\nu^4 + 20\nu^5 - 4\nu^6)\rho^3 \\ &\quad + (405 - 702\nu + 567\nu^2 - 276\nu^3 + 83\nu^4 - 14\nu^5 + \nu^6)\rho^4,\end{aligned}$$

where α_1 and α_2 are positive for $\rho > 1$ and $\nu \in [-1, 1]$. The isotropization coefficient can then be expressed as in Eq. (4):

$$\alpha = -\frac{k}{\mu_0} \left[\left(\kappa_1 + \frac{3}{2} \right) \alpha_1 + \left(\mu_1 + \frac{3}{2} \right) \alpha_2 \right].\tag{S15}$$

As defined here, α increases as $\Delta\phi$ decreases, since κ_1 and μ_1 diverge and μ_0 vanishes. Specifically, given the dependence of the elastic parameters with the area fraction $\Delta\phi$ for Hertzian interactions in Eq. (S13), we can expand Eq. (S15) in powers of $\Delta\phi \ll 1$. In approximating s to 0.5 and t to 1, we find

$$\alpha = \alpha^{(0)}(\Delta\phi)^{-2} + \alpha^{(1)}(\Delta\phi)^{-3/2} + \mathcal{O}((\Delta\phi)^{-1}),\tag{S16}$$

where

$$\begin{aligned}\alpha^{(0)} &= \frac{\phi_c k}{M} \frac{(\rho - 1)^3}{\rho} \frac{4 - 2\rho + \rho^2}{(4 + \rho + \rho^2)^2} t, \\ \alpha^{(1)} &= \frac{\phi_c k}{K} \frac{\rho - 1}{\rho(4 + \rho + \rho^2)^3} \left[6(\rho - 1)^3 (8 + 4\rho + 3\rho^2) t + (64 + 36\rho + 81\rho^2 + 16\rho^3 + 18\rho^4 + \rho^6) s \right].\end{aligned}$$

Consequently, the theoretical expression of α diverges at the transition and scales as $(\Delta\phi)^{-2}$. This scaling is basically the one of μ_1 times the one of $1/\mu_0$. However, as we see in Fig. S7(a), at intermediary $\Delta\phi$, there is a crossover from a slope -2 to a slope -1.5 , due to the scaling of ν with $\Delta\phi$ [Eq. (S14)]. This crossover happens quicker when $r_{\text{out}}/r_{\text{in}} \gtrsim 1$, which explains why the black curve in Fig. 4(a) has an approximate slope slightly larger than -2 .

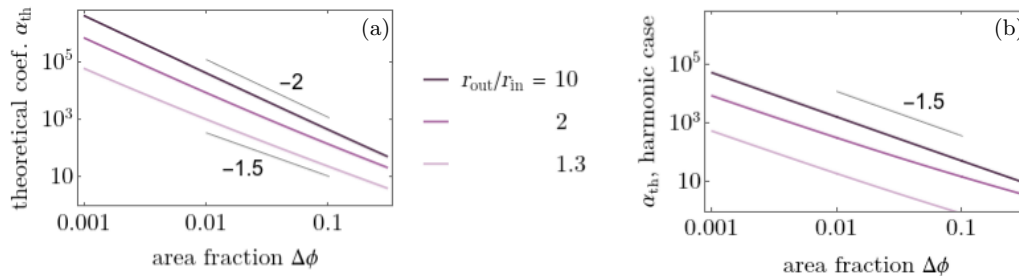


FIG. S7. **The scaling of α from Eq. (4) with $\Delta\phi$ varies with $r_{\text{out}}/r_{\text{in}}$.** For area fractions $\Delta\phi \in [10^{-3}, 10^{-1}]$, the exponent varies from -2 when $r_{\text{out}}/r_{\text{in}} = 10$, to -1.5 when $r_{\text{out}}/r_{\text{in}} = 1.3$. The dependence with $\Delta\phi$ is obtained by using the lowest-order expressions of the elastic parameters in Eq. (S13). (a) Hertzian case, (b) harmonic case.

Harmonic interactions. For harmonic disk interactions $\mathcal{V} \sim k\delta^2$, Eq. (S11) has coefficients $K \simeq 0.3$, $s \simeq 0$, $M \simeq 0.2$ and $t \simeq 0.5$ [5]. This translates into

$$\alpha_{\text{har}} = \alpha^{(0)}(\Delta\phi)^{-3/2} + \alpha^{(1)}(\Delta\phi)^{-1} + \mathcal{O}((\Delta\phi)^{-1}), \quad (\text{S17})$$

with identical $\alpha^{(0)}, \alpha^{(1)}$ coefficients. At a given low $\Delta\phi$, this yields an isotropization effect that is substantial yet weaker than in the Hertzian case, see Fig. S7(b).

III. MEAN-FIELD ELASTO-PLASTIC MODEL

Here we discuss the model introduced in Eq. (6) and the derivation of Eq. (7) from it. We choose to base our description on the standard mean-field Hébraud-Lequeux model due to its tractability and widespread use. While this simple model does not accurately capture all quantitative aspects of the yielding transition [9], we merely use it to provide a proof of principle that a change in the local rules of stress propagation around a shear transformation can affect the macroscopic characteristics of this transition. Specifically, we discuss the steady state behavior of the mean stress

$$\langle \sigma \rangle = \int_{-\infty}^{+\infty} \sigma P(\sigma) d\sigma \quad (\text{S18})$$

as a function of the imposed shear rate $\dot{\gamma}$.

In the standard Hébraud-Lequeux model [the $b = 0$ case of Eq. (6)], each region of the amorphous solid drifts towards higher stresses σ due to the externally imposed stress current $\mu\dot{\gamma}$, and starts to yield with a finite probability as soon as its stress exceeds a threshold σ_c . In this section we rescale all stresses by σ_c and thus set $\sigma_c = 1$. We denote by Γ the rate at which shear transformations occur in the system and use the mean shear transformation time τ introduced in the main text as our time unit (*i.e.*, $\tau = 1$). In the Hébraud-Lequeux description, such shear transformations push the region of interest towards or away from this threshold with equal probability as implied by the $\sigma \rightarrow -\sigma$ symmetry of a Γ diffusion term in Eq. (6). We reason that the build-up of compressive stresses in the material resulting from stress isotropization near unjamming hampers local yielding events driven by the imposed shear stress $\mu\dot{\gamma} > 0$. We thus model this effect by the simplest possible Γ -dependent drift away from the $\sigma = 1$ yielding threshold, corresponding to the b term of Eq. (6).

Solving Eq. (6) in the stationary state with boundary conditions $P(\pm\infty) = 0$ as well as matching the values of P and $\partial_\sigma P$ on either side of the points $\sigma = -1, 0, 1$ while holding Γ constant yields a solution $P_\Gamma(\sigma)$. Imposing the normalization condition $\int_{-\infty}^{+\infty} P_\Gamma(\sigma) d\sigma = 1$ on this solution yields the following self-consistency condition on Γ :

$$a = \frac{x^2}{2} + y^{-1} \left[1 + x\sqrt{1 + \left(\frac{xy}{2}\right)^2} \right] \frac{\frac{xy}{2} + \sqrt{1 + \left(\frac{xy}{2}\right)^2} \tanh \frac{y}{2}}{\frac{xy}{2} \tanh \frac{y}{2} + \sqrt{1 + \left(\frac{xy}{2}\right)^2}}, \quad (\text{S19})$$

where we have defined

$$x = \sqrt{a\Gamma} \quad \text{and} \quad y = \frac{\mu\dot{\gamma}}{a\Gamma} - b. \quad (\text{S20})$$

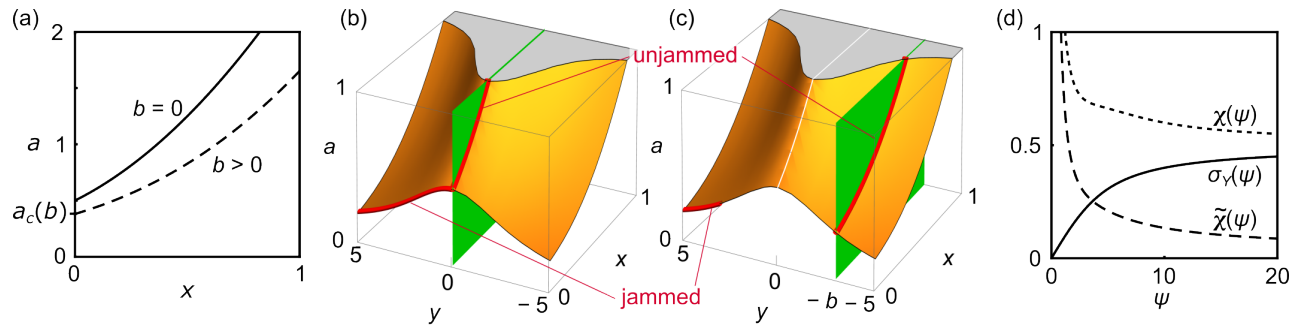


FIG. S8. **Graphical illustration of the nonlinear equations involved in the mean-field elastoplastic model.** (a) No-flow, liquid-state self-consistency condition obtained by setting $\mu\dot{\gamma} = 0$ (*i.e.*, $y = -b$) in Eq. (S19). For a given value of the parameter a , this curve allows us to read out the corresponding value of x . (b) Illustration of the change of solution of Eq. (S19) when transitioning from an unjammed (liquid-like) to a jammed (solid-like) state in the standard Hébraud-Lequeux $b = 0$ case. The yellow surface materializes the solutions of Eq. (S19). For a given value of a , all the solutions in the plane with altitude a are accessible. Those with zero flow are given by the intersection from this yellow plane with the green $\dot{\gamma} = 0 \Leftrightarrow y = 0$ plane (“unjammed” red line). Imposing a flow in the $\dot{\gamma} > 0$ direction makes this solution move away from the green plane and along the line defined by the intersection of the yellow surface and the horizontal plane (*i.e.*, the plane of constant a). In cases where $a < 1/2$, a change of sign of $\dot{\gamma}$ is accompanied by a discontinuous jump of the value of y . The $\dot{\gamma} = 0^+$ solutions are marked by the “jammed” red line. (c) Selection of the solutions in the $b > 0$ case. Starting from a large value of a , we can follow the “unjammed” red line at the intersection of the yellow surface and the $y = -b$ plane. This line ends at $a = a_c(b)$, which marks the jamming transition. This value of a is smaller than in the $b = 0$ case, and does not correspond to the top of the bump in the yellow surface. For values of a lower than $a_c(b)$, the $\dot{\gamma} > 0$ branch is obtained by jumping to the $y > 0$ part of the yellow surface. Unlike in the $b = 0$ case, such a jump is required even in the critical case $a = a_c(b)$. The line of jammed solutions highlighted in red gives the $\dot{\gamma} \rightarrow 0^+$ limit of these solutions. The discussion of the text is focused on the neighborhood of this line. (d) Plots of the quantities defined in Eqs. (S25) and (S26).

For a given externally imposed shear rate $\dot{\gamma}$, solving Eq. (S19) yields a value for Γ , and thus information about the flow state of the system.

We first consider the case of a system without externally imposed flow ($\dot{\gamma} = 0$). The value of y is then known, and Eq. (S19) must be solved for x . As shown in Fig. S8(a), it allows for $x > 0$ solutions only when a is larger than a critical value

$$a_c(b) = \frac{1}{b} \tanh \frac{b}{2}. \quad (\text{S21})$$

The parameter a was originally introduced in Ref. [10] as a proxy for the density of the system, where denser systems correspond to lower values of a . This gives rise to the following standard interpretation for the existence of a $x > 0$ solution to Eq. (S19):

- Parameter regimes where this solution exists correspond to low-density systems, namely those with $a > a_c(b)$. Such systems display a non-vanishing steady-state value for their plastic activity Γ . In the case $b = 0$, such systems are usually interpreted as unjammed fluids, and we extend this interpretation to the case $b > 0$.
- Parameter regimes where this solution does not exist represent high-density systems, namely those with $a < a_c(b)$. These systems display a vanishing value of Γ in the case of a vanishing driving $\mu\dot{\gamma} = 0$. Imposing a small, positive value of $\mu\dot{\gamma}$ does however result in a non-vanishing Γ and a discontinuous jump in the mean stress $\langle \sigma \rangle$, likening systems in this regime to jammed yield-stress fluids.

In our model, the former of these two cases gives rise to a linear, Newton-like rheology similar to that derived from the standard Hébraud-Lequeux model. As the parameter a is lowered under $a_c(b)$ however, this solution ceases to exist and the system transitions to another solution of Eq. (S19) [Fig. S8(b-c)]. For finite values of b , the $\dot{\gamma} \rightarrow 0^+$ asymptotics of this solution is given by

$$x = \sqrt{\frac{\mu\dot{\gamma}}{b + \psi}} + \mathcal{O}(\mu\dot{\gamma}) \quad (\text{S22a})$$

$$y = \psi \left(1 + \frac{\sinh \psi + \psi}{\sinh \psi - \psi} \times \sqrt{\frac{\mu\dot{\gamma}}{b + \psi}} \right) + \mathcal{O}(\mu\dot{\gamma}), \quad (\text{S22b})$$

where the function $\psi(a)$ depends only on parameter a and is defined through

$$a = \frac{1}{\psi} \tanh \frac{\psi}{2} \quad \text{and} \quad \psi > 0. \quad (\text{S23})$$

Thus ψ is equal to 0 when $a = 1/2$ and monotonically increases to $+\infty$ as a decreases to 0. The resulting relationship between stress and strain rate is of the yield stress type, with

$$\langle \sigma \rangle = \sigma_Y(\psi) + \frac{\chi(\psi)}{\sqrt{b + \psi}} \sqrt{\mu \dot{\gamma}} + \mathcal{O}(\mu \dot{\gamma}), \quad (\text{S24})$$

where the yield stress and susceptibility are respectively given by

$$\sigma_Y(\psi) = \frac{1}{2} \coth \frac{\psi}{2} - \frac{1}{\psi} \quad (\text{S25a})$$

$$\chi(\psi) = \frac{1}{\psi} + \frac{5 + \cosh \psi - 3\psi \coth(\psi/2)}{2(\sinh \psi - \psi)} \quad (\text{S25b})$$

and are plotted in Fig. S8(d).

As illustrated in Fig. S8(b-c), unlike in the Hébraud-Lequeux model the transition between the unjammed and jammed state in our $b > 0$ model is of the first order. This is in contrast with the transition encountered in the Hébraud-Lequeux model, which is of the second order and displays a critical regime where $\langle \sigma \rangle \propto (\dot{\gamma})^{1/5}$. This critical regime is never manifested in our $b > 0$ model, and the rheology at the transition is given by (noting that $a = a_c \Rightarrow \psi = b$):

$$\langle \sigma \rangle_{\text{at unjamming}} = \sigma_Y(b) + \tilde{\chi}(b) \sqrt{\mu \dot{\gamma}} + \mathcal{O}(\mu \dot{\gamma}), \quad (\text{S26})$$

where $\tilde{\chi}(b) = \chi(b)/\sqrt{2b}$ is plotted in Fig. S8(d). According to Eq. (S26), at the unjamming transition the $b > 0$ system displays the same yielding behavior and Herschel-Bulkley exponent as in the jammed state. The small- $\dot{\gamma}$ expansion scheme leading to Eq. (S26) breaks down at $b = 0$, which is apparent in the divergence of $\tilde{\chi}(b)$ for $b \rightarrow 0^+$. Consistent with our previous discussion, this divergence signals the presence of the Hébraud-Lequeux critical regime. Equation (7) of the main text is a summarized version of Eq.(S26).

We note that the difference in critical regime discussed here is fundamentally due to a loss of the $\sigma \rightarrow -\sigma$ symmetry in our model, which implies a change in the order of the unjamming transition. We can speculate that some version of this difference will subsist even in more sophisticated models, *i.e.*, that it is a robust feature beyond the assumptions and simplifications made here. We however expect that the specific values of the Herschel-Buckley exponents discussed here will change when, *e.g.*, relaxing our mean-field assumption.

-
- [1] A. P. Thompson *et al.*, [Comp. Phys. Comm.](#) **271**, 108171 (2022).
 - [2] H. P. Zhang and H. A. Makse, [Phys. Rev. E](#) **72**, 011301 (2005).
 - [3] H. A. Makse, N. Gland, D. L. Johnson, and L. M. Schwartz, [Phys. Rev. Lett.](#) **83**, 5070 (1999).
 - [4] H. A. Makse, N. Gland, D. L. Johnson, and L. M. Schwartz, [Phys. Rev. E](#) **70**, 061302 (2004).
 - [5] C. S. O'Hern, L. E. Silbert, A. J. Liu, and S. R. Nagel, [Phys. Rev. E](#) **68**, 011306 (2003).
 - [6] C. F. Schreck, C. S. O'Hern, and L. E. Silbert, [Phys. Rev. E](#) **84**, 011305 (2011).
 - [7] L. E. Silbert, D. Ertaş, G. S. Grest, T. C. Halsey, D. Levine, and S. J. Plimpton, [Phys. Rev. E](#) **64**, 051302 (2001).
 - [8] F. Benoist, G. Saggiorato, and M. Lenz, [Soft Matter](#) **19**, 2970 (2023).
 - [9] A. Nicolas, E. E. Ferrero, K. Martens, and J.-L. Barrat, [Rev. Mod. Phys.](#) **90**, 045006 (2018).
 - [10] P. Hébraud and F. Lequeux, [Phys. Rev. Lett.](#) **81**, 2934 (1998).